

Modelling and experimental studies of rotating flows in part-filled vessels: wetting and peeling

K.S.Sujatha¹, M.F.Webster^{1*}, D.M.Binding² and M.A. Couch²

Institute of Non-Newtonian Fluid Mechanics,
¹Department of Computer Science,
University of Wales, Swansea, SA2 8PP, UK.

²Department of Mathematics,
University of Wales, Aberystwyth, UK.

SUMMARY

The main purpose of this paper is to corroborate numerical modeling and experimental results for rotating flows with free-surfaces. This work is associated with dough-kneading and the validation of surface positions. Free surface flow in a rotating cylinder is investigated when a fluid is stirred in a cylindrical-shaped vessel with a stirrer attached to the lid of the vessel. The stirrer may be placed in either concentric or eccentric position with respect to the axis of the vessel. Both horizontal and vertical orientations of the vessel are studied at various rotational speeds. Wetting and peeling at solid boundaries is incorporated to achieve realistic simulations. Experimental visualization for free-surfaces involve laser scatter technology and contemporary imaging methods for more complex flows. A video capture technique is used to determine peeling stresses experimentally, which compares well with the stress obtained from numerical computations. Close agreement is obtained between numerical and experimental flow fields and free surface profiles. Model fluids employed are various percentage concentrations of CMC, which have shear-thinning properties.

KEY WORDS: Dough-kneading, laser scatter, free-surface, Lagrangian-Eulerian, non-Newtonian, wetting and peeling.

1. INTRODUCTION

This study is part of a research programme aimed at improving the kneading of dough in industrial dough mixers. The results from numerical modeling are validated with equivalent experimental results conducted at UW Aberystwyth, addressing calculation and visualisation of free-surface flows associated with part-filled rotating cylindrical-shaped vessels. These are scaled versions of actual commercial mixers (termed model mixers). New techniques for wetting and peeling have been developed to model this complex free-surface flow. Experiments are conducted with peeling of dough from solid surfaces so that the data resulting from this study is then used in the simulation with appropriate conditions at the solid/fluid interface.

* Author for correspondence

In the literature, different methods have been used to model free-surfaces. The Lagrangian approach comprises of moving mesh systems, following the movement of the fluid (eg. Marker Particle method [1]). This method requires frequent re-meshing due to the distortion of the domain in the course of time. Alternatively, with Eulerian-based methods, no re-meshing is required as the governing equations are solved in a larger domain than is actually occupied by the fluid, distinguishing between wet and dry regions (eg. Volume of Fluid method (VOF) of Hirt and Nichols [2]). The original VOF method employed a finite difference scheme. This method was later extended by various investigators to solve a variety of problems, such as mould-filling and metal casting, that involved complicated boundaries. A VOF method, based on finite element techniques was also developed, but was only applied to relatively simple problems, due to the complexities involved [3]. Subsequently, an improved version of the VOF method has been developed, in which the flow field is treated as a two-phase system. In this method, the regions filled with fluid are assumed to lie within a single phase. The dry region, separated by the free surface boundary, is considered as a second phase. It is assumed that the dry regions consist of a virtual fluid, where artificial physical properties are imposed. Thus, this scheme is termed a pseudo-density method [4]. To avoid using artificial physical properties, Nassehi [5] treated the dry section as a compressible fluid. Arbitrary Lagrangian-Eulerian methods combine the respective advantages of both Lagrangian and Eulerian methods [6]. A mixed Lagrangian-Eulerian method was developed by Ramaswamy [7] for calculating the transient dynamics of incompressible, viscous fluids with free-surfaces.

On the experimental side, the application of flow visualization to record the streamlines associated with model fluid flows, using traditional laser scatter techniques with stills photography, has been well documented in the literature; see for example, Cochrane, Walters and Webster [8], Boger [9] and Evans and Walters [10]. Prakash and Kokini [11] have performed studies using LDA (Laser Doppler Anemometry) to determine the velocity vectors associated with flows in model mixers. Such studies used the velocity calibrations to estimate shear-rate distribution in the mixer. In the literature, notwithstanding the work on peeling of adhesives, very limited research has been reported with respect to the peeling of dough (Dobraszczyk [12]).

The first part of this work, dealing with numerical and experimental studies on filled geometries, has been published elsewhere [13-17]. The present study concentrates on the modeling and visualization of unsteady free-surface flows encountered in the wet phase of dough kneading. Two different dough mixer designs are investigated, both with a single rotating stirrer. This may be placed either in a concentric or eccentric arrangement, with respect to the axis of the vessel. As an alternative to the more common mixer operation, the motion is assumed to be driven by the rotation of the vessel. This is a convenience only, and simply aids in the representation within the modelling. The mixer is considered both in a vertical (r, θ, z), 3D mode, and horizontal (r, θ) orientation (2D mode), and to be partially-filled during the process. Model fluids, that is, syrup (Newtonian), and CMC(1%), CMC(2%), and CMC(3%) for inelastic fluids have been utilised.

The simulation employs a Taylor-Galerkin finite element formulation for the generalised Navier-Stokes equations. An arbitrary Lagrangian-Eulerian scheme is adopted to accommodate free surface movement. A fixed finite element mesh covers

the whole domain, that is divided dynamically into two different sections: one wet and another dry. The position of the free surface defines the perimeter of the fluid region. The solution of the field variables is activated only within the wet fluid zone. Wetting and peeling boundary conditions are applied at fluid-solid interfaces to match the surface profiles extracted from the experiments.

The experimental components of the work incorporate some elements of laser scatter technology, but also utilize more contemporary imaging methods. The main goal is essentially to provide validation for the numerical simulations, but evolving to encompass most of the characteristics of realistic fluids. The model fluids developed for this purpose are designed to be appropriate in nature for the process (i.e., Newtonian or inelastic). These are characterised rheologically, so that the fluid parameters used in the simulations can be matched with those of the experiments, accordingly. For surfaces with symmetrical profiles, an illuminating plane of laser light is used to facilitate the visualisation. However, for more complex surfaces with 3D relief, high-resolution digital camera images, taken from four radially distributed views, are exploited. In order to capture the transient nature of the flows, additional video footage with digital data capture is employed. Using a torque transducer, torque history is recorded and from that, distinct modes of mixing in the process may be identified.

Experiments were also conducted with peeling of dough from solid surfaces. This involves a video capture technique, to determine the stress associated with the peeling of dough from a surface by visualising the surface area in contact with the plates. These tests are conducted for both bread and biscuit doughs. From such experiments, peeling stress may be established as a function of speed, compressive load, material roughness, dough water content, mixing time and dough type.

2. NUMERICAL SIMULATION

2.1 Governing equations and numerical scheme.

The generalized momentum and continuity equations for viscous incompressible isothermal flow, may be expressed as:

$$\rho U_t = \nabla \cdot (\mu \nabla U) - \rho U \cdot \nabla U - \nabla P + \rho g, \quad (1)$$

$$\nabla \cdot U = 0, \quad (2)$$

where variables (U) and pressure (P) are defined over space and time with time derivative represented as (U_t). Material properties are given via density (ρ) and viscosity (μ). A Carreau-Yasuda model, represented by equation (1) below, is employed to describe the shear-thinning behaviour of the viscosity μ ,

$$\mu = \frac{\mu_0 - \mu_\infty}{1 + (\lambda \dot{\gamma})^m} + \mu_\infty, \quad (3)$$

where μ_0 is a reference viscosity at low shear-rates and μ_∞ is an asymptotic value of viscosity at large shear rates; $\dot{\gamma} = 0.5\sqrt{I_2}$ with the second invariant I_2 of the rate-of-strain tensor, m is a powerlaw index and λ is a material constant.

For convenience of representation, we adopt non-dimensional variables, via scales of reference as follows:

$$x^* = \frac{x}{L}, \quad u^* = \frac{u}{V}, \quad \mu^* = \frac{\mu}{\mu_c}, \quad t^* = \frac{V}{L} t, \quad P^* = \frac{L}{\mu_c V} P \quad (4)$$

where L , V and μ_c are characteristic length, velocity and viscosity, respectively. We adopt L as the diameter of the stirrer, V the speed of the vessel and μ_c a zero shear-rate viscosity (typically, 1.05Pa.s). This leads to a Reynolds number, the non-dimensional group involved, and the coefficient for the gravitational term ' F ' defined as:

$$\text{Re} = \frac{\rho L V}{\mu_c}, \quad F = \frac{\rho L^2 g}{\mu_c V} \quad (5)$$

where ρ is the fluid density. Henceforth, we discard the $*$ notation for ease of presentation. To be specific, in the present work, we take $m = 0.6$ and $\lambda = 0.083s$. Substitution of the above dimensionless variables into equation (1) yields the non-dimensional generalized Navier-Stokes equations,

$$\text{Re} U_t = \nabla \cdot (\mu^* \nabla U) - \text{Re} U \cdot \nabla U - \nabla P + F g, \quad (6)$$

$$\nabla \cdot U = 0. \quad (7)$$

A semi-implicit time-stepping procedure, namely, a Taylor-Galerkin/pressure-correction finite element scheme is employed to solve the field equations relating to the conservation of mass and momentum. The time-stepping scheme is derived through Taylor series expansions up to second-order in time-step and a two-step predictor-corrector scheme is assumed. This, in conjunction with a second-order pressure-correction method, to accommodate the incompressibility constraint, produces a fractional-staged equation system. This system is solved over three distinct phases within a single time-step. A semi-implicit Crank-Nicolson treatment is adopted in time to discretise the diffusion terms. A Galerkin finite element spatial discretisation renders a fully-discrete system. The choice is made of piecewise continuous quadratic functions for velocity, and linears for pressure, based upon tetrahedral elements in three dimensions (and equivalently, triangles in two dimensions). Further details on the analysis are published extensively in the literature [18-20]. The algorithm has three fractional-stages per time-step interval, $[t^n, t^{n+1}]$, of size Δt , as follows:

Stage 1: From initial velocity and pressure fields, non-divergence-free $U^{n+\frac{1}{2}}$ and U^* fields are calculated via a two-step predictor-corrector procedure. The corresponding equations are solved iteratively by a Jacobi method.

Stage 2: Using U^* , calculate the pressure difference ($P^{n+1} - P^n$) via a Poisson equation, applying a direct Choleski method of solution. The matrix K is symmetric, sparse and banded in structure. Being independent of the solution, it may be reduced efficiently once only for a fixed mesh, at the outset of the time-stepping procedure.

Stage 3: Using U^* , and pressure difference ($P^{n+1} - P^n$), determine the divergence-free velocity field U^{n+1} by Jacobi iteration.

Adopting quadratic $\phi_j(x)$, and linear $\psi_j(x)$ interpolations, $U(x,t)$ and $P(x,t)$ may be expressed as:

$$U(x,t) = U_j(t)\phi_j(x), \quad P(x,t) = P_j(t)\psi_j(x).$$

The equation stages in fully-discrete form may be represented in the following form:

stage 1a:

$$\left[\frac{2Re}{\Delta t}M + \frac{1}{2}S_u\right](U^{n+\frac{1}{2}} - U^n) = \{-[S_u U + \text{Re}N(U)U] + L^T P + F\phi_i g\}^n \quad (8)$$

stage 1b:

$$\left[\frac{Re}{\Delta t}M + \frac{1}{2}S_u\right](U^* - U^n) = [-S_u U + L^T P + F\phi_i g]^n - \text{Re}[N(U)U]^{n+\frac{1}{2}} \quad (9)$$

stage 2:

$$K(P^{n+1} - P^n) = -\frac{2}{\Delta t}LU^* \quad (10)$$

stage 3:

$$\frac{Re}{\Delta t}M(U^{n+1} - U^*) = \frac{1}{2}L^T(P^{n+1} - P^n) \quad (11)$$

where U^n , U^{n+1} , P^n and P^{n+1} are nodal vectors of velocity and pressure at time t^n and t^{n+1} respectively; $U^{n+\frac{1}{2}}$ is the half time-step nodal velocity vector; U^* is an intermediate nodal velocity vector introduced in step 1b; M , S_u , $N(U)$, K and L are mass matrix, momentum diffusion matrix, convection matrix, pressure stiffness matrix and divergence-pressure gradient matrix, respectively. The above matrices defined over an (r,θ,z) co-ordinate system are expanded in refs. (15,16).

Typical meshes used for the two and three-dimensional problems addressed are demonstrated in Fig (1). For the vertical mixer orientation in three-dimensions, a cylindrical vessel is considered with a concentric or eccentric located stirrer with respect to the axis of the vessel. The rotation of the outer vessel drives the fluid and the vessel is fixed to a lid at the top. In this case, tetrahedral elements are employed. To create a three-dimensional finite element mesh, first each brick element is formed, which is then divided into six tetrahedra. For the concentric arrangement (1d), this leads to 6000 tetrahedral elements, 9240 velocity nodes and 1320 pressure (vertex) nodes. For the eccentric case (1c), there are equivalently 3600 elements, 5270 velocity nodes 840 pressure nodes. In the simulation runs, the vessel is taken as sixty percent full by volume. The outer vessel, attached to the bottom plate, rotates at different rotational speeds and the top is held stationary. For the two-dimensional horizontal orientation (1a), typically the flow geometry is discretised into a mesh with 240 triangular elements, 520 velocity nodes and 140 pressure nodes.

2.2. Free-surface tracking and wetting/peeling procedures.

An arbitrary Lagrangian-Eulerian method has been employed to model free-surfaces. The flow domain is divided into two distinct parts: one wet and another dry. Residing only within the wet-fluid zone, finite element calculations are performed to

obtain the field variables, such as velocity, pressure and stress. After each movement of the free-surface, the field solution is improved by introducing sub-iterations/sub-time step. In this manner, separate time-step control is enforced on the surface movement from that for the full wet domain computation. In each Taylor-Galerkin phase, typically one hundred sub-time steps are performed.

The fluid surfaces may consists of many particles and the surface profiles are obtained by tracking their positions. A well-established Runge-Kutta scheme is adopted to track the particle positions. This may be represented via an explicit Euler step:

$$x_p^{n+1} = x_p^n + \Delta t v(x_p, t^n) \quad (24)$$

where, for particle p , x_p^n is its position at time t^n , $v(x_p, t^n)$ its velocity at x_p^n at time t^n , x_p^{n+1} is a position at time t^{n+1} . This scheme is performed after stage 3 of each time step of the Taylor-Galerkin algorithm, that is, at the end of each time-step cycle. For practical convenience, a small gap is introduced between the first free-surface particle and the cylinder wall, to avoid dealing with stationary particles (no-slip). Typically, between three thousand and six thousand particles are employed to trace the surface.

The particles are moved by the explicit Euler step discussed above in order to obtain their temporal up-dated positions. After moving the surface, the newly wet and dry regions are identified and the status of all nodes is reassigned, whether wet or dry. For elements which are part-wet, material properties are allowed to adjust over a single element. No explicit boundary conditions are imposed on the surface. By assigning appropriate material properties to each Gauss quadrature sample point within an element, the boundary conditions are directly incorporated into the finite element calculations. Therefore, no local re-meshing is required close to the interface. After reassigning node status and material properties, velocity and pressure fields for the new domain are computed at the next time step t^{n+1} . In the present problem, this procedure is repeated until a stable steady-state is reached.

Innovative algorithms to deal with wetting and peeling conditions between the fluid and solid surfaces have been devised, represented diagrammatically in Fig. 2. In the case of vertical-vessel orientation with rotating vessel, Fig. 2(a), wetting occurs at the outer vessel and peeling at the stirrer. Alternatively, in horizontal-mixer orientation, Fig. 2(b), peeling may be observed at the contact point between the advancing surface and the solid boundary, whilst wetting may be observed at the dragging surface and the solid vessel wall. Peeling again arises at the stirrer. Wetting or peeling is detected if a free-surface segment in contact with the solid boundary is stretched/contracted beyond a limiting stretch factor (α), taken from empirical estimation and guided by experimental visualisation. When such a situation arises, the free-surface is constrained by iteratively relaxing the newly calculated position till the stretching criteria is met. Additionally, a check is made to safeguard against particle coalescence and buckling of line segments. In the three-dimensional vertical-vessel problem, wetting is also controlled by the angle (θ) subtended between wall and line-segment, connecting the particle on the wall and the nearest neighbour particle on the same radial line. If this angle were to drop below a predefined threshold, the latter particle is taken as having attached itself onto the wall (the surface is wetted).

For both horizontal and vertical-vessel orientations with one stirrer, a limiting value α of five at the outer vessel is found to be suitable. For the inner stirrer, different values of α have been considered. For vertical-vessel orientation, a static α_{stir} -value of two is reasonably acceptable. The horizontal setting has demanded a more dynamic approach, with α_{stir} -value varying from 1.3 at the outer stirrer section (narrow-gap) to 0.8 for the inner stirrer section (wide-gap). Further detail on the simulation of wetting and peeling is consigned to refs. [22,25].

3. EXPERIMENTAL CONSIDERATIONS

The development and characterization of the model fluids has been considered elsewhere Binding et al. [17] and Couch and Binding [14]. In summary, these fluids are designed to have characteristics similar to those of model doughs, but are intended to be transparent in order to facilitate flow visualization. The two fluids considered in the experimental study are a Newtonian glucose syrup and water solution and a relatively inelastic 1% aqueous solution of CMC. As mentioned above, the parameters used to represent the simulation fluids match those obtained by the characterization of the model fluids.

3.1 Surface visualization

A model mixer, provided by industry, has enabled the process to be studied in a scaled-down and simplified fashion. We have made use of this prototype industrial dough mixer [14,17] to provide a rotating base for the model geometries. This generates turntable speeds of between 25 and 450 rpm and is capable of providing both horizontal and vertical axial orientations. The drive shaft was also equipped with a torque transducer, so that the torque history of a typical mixing run could be recorded. Notably, the time scale of several minutes did not demand specific high-speed capability.

Fig. 3 shows the model geometries considered, reflecting both concentric and eccentric rod positions. Experimentally, the eccentric case has been considered with both one and two rod configurations and is also considered in horizontal orientation (with one rod). Both the cylinders and the stirring rods are fashioned from Perspex, hence facilitating clear visualisation. In the horizontal configuration a flat Perspex lid is included to prevent the progression of the model fluid from the geometry and to provide an end viewing-window, see Fig. 4. In all instances, the rods are held fixed while the cylindrical vessel is rotated, at a fixed angular velocity. Here, within experimental runs, the geometries are half-filled with the various model fluids.

With concentric geometry configurations, the surfaces generated by the model fluids are symmetric about the axis of rotation and can, therefore, be described fully by viewing a slice of the surface along the diameter of the vessel. To provide this view two vertical planes of laser light are generated with laser diodes and beam splitters and projected from either side of the geometry. The surface of the fluid is coated with a thin layer of aluminium powder, so that in darkened conditions it will become brightly illuminated by the projected laser light. To prevent distortion of the surface image, due to the lens effect of the curved surface of the cylinder, the geometry is enclosed in a rectangular tank filled with the same liquid, so that the refraction caused by the

geometry curvature is overcome. A graduated scale is immersed in the model fluid at the geometry diameter viewed, in order to calibrate the scale of the image and to ensure non-linearity is avoided. The development of the surface, from start-up until the fluid reaches a steady speed, is viewed with a conventional video camera and the resulting images are downloaded to PC via standard video capture software and stored digitally. For analysis, the images are stacked in a slide show format and for each picture, the (x, y) coordinates of the surface are recorded at evenly spaced intervals using gridlines.

With the eccentric geometry, the surfaces generated have a more complex 3D relief pattern which, cannot be visualised meaningfully using the laser plane technique outlined for the concentric case. Instead, digital camera images are utilised since the high-quality images they provide give an impression of depth, via colour and shading, required to identify the detail of these surfaces. The rectangular tank is again used to minimise refraction problems and a powerful 2 kW light source, filtered through a diffuser, is found to provide the optimum lighting. To improve the visualisation capability further, the digital photographs are taken from four different viewing angles, radially distributed about the geometry. Photographs are taken from all four views across the relevant speeds, once steady-state conditions have been realised. In addition, to derive an impression of the transient nature of the surface development, video imaging is also employed as outlined above, but with ambient lighting. Although these images do not provide the same clarity and contrast as those of the digital camera, they are sufficiently accurate to demonstrate how the surface develops in time. Essentially within the experimental programme, the same technique is adopted for the two-rod eccentric geometry, except that here (because of the axis of symmetry) only two orthogonal views are necessary. To correspond to the simulations, only a single-rod instance is reported.

The final geometry considered is the eccentric geometry in horizontal orientation. Again, only the one-rod case is reported in this article. For these experiments the surface is viewed through the flat lid of the geometry, so no distortion of the image takes place. The model fluid is dyed blue to improve the visibility of the surface, which is difficult to observe otherwise, due to the fact that it is parallel to the plane of the view. As the surface structure is simpler than that of the vertical case, it can be visualised using the video camera alone. The camera is placed at a distance of approximately 0.3m away from the geometry. This provides a sharper image (more important) than placing the camera at a distance necessary to eliminate the effect of perspective (less important) on the images of the surface. In this manner, both transient and steady-state surfaces may be recorded.

A peeling apparatus was devised to simulate the peeling of dough away from the surface of the mixing bowl in a more controlled fashion. This was intended to support the numerical work by supplying peeling stress as a function of stress and/or strain-rate. The apparatus incorporated a prototype capillary rheometer, that was modified to provide a simple example of the mechanism behind dough peeling. The ram of the instrument was used to provide constant velocity vertical motion of a steel upper-plate at speeds ranging from 0.05 to 2.5 mm/s. A load cell and monitoring arrangement, attached to a perspex lower-plate were used to determine the load history generated by a dough sample sandwiched between the plates. The area of contact between the sample and plates was determined from video footage, which coupled with the load histories, enabled the estimation of developing stresses on the surface.

4 RESULTS

For both horizontal and vertical-vessel orientations, simulations and experiments have been conducted at various speeds, namely, 25, 50 and 100 rpm ($Re=4, 8$ and 16), which are of relevance to the process.

4.1 Vertical-vessel orientation

A cylindrical vessel with a stirrer, placed concentric and eccentric to the axis of the vessel, has been considered for three-dimensional vertical vessel orientation. For the concentric geometry, the surface formed by the model fluid is smooth, regular, symmetric and essentially parabolic in cross section, although there is obviously some deviation from this form due to the presence of the central stirrer. As the rotational speed is ramped up, the height of the fluid at the wall naturally increases relative to the minimum height near the rod, due to the impartation of rotational kinetic energy into the fluid. Since the surface is symmetric, the geometry is sliced at the centre along the axis and the surface positions are plotted in two dimensions. Free-surface profiles are plotted at steady-state for different speeds, namely, 25, 50 and 100 rpm ($Re = 4, 8$ and 16), and compared with the equivalent experimental plots. Fig. 5(a) demonstrates a typical comparison set. In Fig. 5(a), a slight discrepancy (about 7% at maximum, taken with reference to the height of the vessel, mid-way between stirrer and vessel) is noted between experimental and simulation steady profiles at the highest speed of 100 rpm ($Re=16$). This deviation may be due to the constant value of limit parameters chosen for wetting-and-peeling conditions, irrespective of different rotational speeds involved. The standard speed of the process is 50 rpm ($Re=8$) and limiting parameters are chosen so as to match results at this speed. Figure 5(b) shows the development of the fluid free-surface in time against experimental results. The fluid motion starts from rest and as time progresses through a rise time of just over a second, the fluid wets the outer wall and peels away from the stirrer, due to the centrifugal force. The final steady position is noted to take up a parabolic shape.

Particle positions obtained from simulation and experiments for the concentric situation are represented in three-dimensional mode in Fig. 6. The speeds chosen are 25, 50 and 100 rpm ($Re= 4, 8$ and 16). These images are created by imposing the particle positions on a three-dimensional frame. Results from numerical simulations are demonstrated in Fig. 6(a), (b), (c) and equivalent experimental results in Fig. 6 (e), (f) and 9(g). It is apparent that as speed increases, the depth increases. Fig. 6(d) at $Re=8$ (50 rpm), illustrates the simulation results with particles on the surface.

The surface patterns are much more complex and irregular for the eccentric stirrer location than for their concentric counterparts. These are illustrated in Fig.7. There is rise and fall of the surface position about the stirrer, varying continuously around the stirrer. The most discernable feature observed is a groove (or fin) that forms in the wake of the rod. The maximum height rise of the fluid surface at the wall relative to the minimum (near the central axis of the geometry), is considerably less than that observed for the concentric case at comparable speeds. This can be attributed to the dissipation of energy in the shear flow that occurs around the rod, but mainly between

the rod and the wall. For the two-rod concentric case this effect is exacerbated. A comparison between free-surface profiles obtained from simulation and experiment for the eccentric one-stirrer geometry is provided in figure 7(a-e). Since the surface shape is highly complex, exact comparison is difficult and, only qualitative comparison is possible. A plot of the surface shape (height) from simulation (speed=50rpm) is illustrated in Fig. 7(a-c) and an equivalent plot from experimental visualisation is demonstrated in Fig. 7(d-e). Figs. 7a and 7b illustrate two different viewing angles of the surface, and Fig. 7c depicts the height contours of the surface. The maxima and minima in height are represented by red and blue colours, respectively. Stirrer position in fig. 7c is identical to that shown in Fig. 7a. With reference to Fig. 7a, in the vicinity of the stirrer, there is a dip at the backside of the stirrer, whereas the fluid attempts to climb on the stirrer at the front. On the outer vessel, there is a dip in the front and a rise at the backside, as apparent in Fig. 7e.

From a particle lying close to the stirrer and its immediate neighbour on the same radial line, for example, particles 'H' and 'G' from Fig. 2(a), the local stress and stretch are computed and plotted against time in Fig.8. As the vessel rotates, the second particle (G) pulls away from the first (H), due to the action of centrifugal force. As the distance between particles increases, the stretch increases, until a critical level is reached. This is known as the critical peeling stress. Beyond this phase, the fluid peels from the stirrer (first particle H departs the surface), so that the stretch decreases. The local stress follows the same pattern as that of the stretch. The match in pattern of stretch and peeling-stress time-trace indicates that either would be equally as valid as monitoring criteria within the algorithm. The flexibility of the techniques employed, in their ability to deal with these most complex of boundary interaction phenomena (that would extend equally to slip), highly commends this transient approach.

A typical torque-time trace for inelastic fluids from simulation for the eccentric one-stirrer geometry is demonstrated in Fig. 9(a), where torque is an integrated quantity of the rate-of-work done in the whole field (see refs. [15,16]). A similar curve is presented in fig. 9b from experimental measurements for dough. The periodic nature of the torque-time trace is apparent in both figures. Ignoring the start-up phase for comparison purposes, essentially, it is only the first period of up to 75 seconds, and third period around 100 seconds, where the dough is in contact with stirrer and vessel. Only these periods are categorised in the modeling. In the simulations with model fluids, torque levels are halved from the experiments and some similarity may be gleaned out, in periodic rising trend, with those of the experimental mixing periods. Hence, qualitatively, the simulation results are a reasonable physical reflection of this mode of the mixing process. From the experimental torque-time trace (Fig. 9 (b)), it was found that four distinct modes of mixing could be observed and correlated with the torque response. These provide an overview of the complete mixing cycle and an important link to the physical problem. Typically, just after the mixer was started and the raw ingredients came together, a type of mixing was initiated where the dough was continually being pushed onto and pulled off the walls of the bowl by both stirring rods. This mode conformed to high torque levels with large fluctuations corresponding to the peeling of the dough away from the wall. This type of mixing was desirable because, as the dough was pulled away from the wall by the rods, it experienced elongation, an important component of dough kneading and an efficient mixing mechanism. The second mode of mixing occurred when a portion of dough came away from the main mix and remained on the turntable between the rods. Obviously this dough portion did not receive adequate mixing and the mode could, therefore, be

regarded as inefficient. Later in the mixing cycle, all of the dough would climb up a single stirring rod (Weissenberg effect) and be sheared between the rod and the wall as the rod processed about the vessel. Although for this mode the resulting torque levels were high, the fluctuations were small compared to the first mode. Thus, this mode represented inefficient mixing, since only the dough between the rod and wall was actually being sheared. Further, it was recognised that shearing is a less efficient form of dough kneading than that promoted through elongation. The final mode encountered, occurred late in the mixing cycle, when all of the dough came away from the wall of the mixer to be carried around on the two rods. As may be anticipated, this state corresponded to very low levels of torque and represented totally inadequate mixing. Considering the mixing process as a whole the first mode lasted for less than half of the total mixing time and so the process could be made considerably more efficient in terms of time and energy consumption by eliminating the other modes. Within the wider programme of work reported elsewhere [21,22], the model mixer was subsequently modified, by fixing three baffles (of triangular cross section) to the wall of the mixer at even intervals. With the addition of the baffles it was found that the inefficient modes of mixing were eliminated from the mixing process. This left only the mode where the dough was continuously pushed onto and pulled off from the wall by the rods. This state of affairs is taken to represent efficient kneading. We refer also to refs. [23,24], that specifically deal with different mixer designs for viscoelastic materials and their influence upon kneading efficiency.

4.2 Horizontal-vessel orientation

Next, we switch attention to the comparison of results from the corresponding scenario, when the vessel is held in a horizontal orientation. Deformation patterns of the free-surfaces, whilst the vessel rotates a quarter of a rotation, two rotations and after twenty rotations are illustrated in Figs. 10(a-f). Figs. 10 (a), (b) and (c) represent results from simulation at a typical speed of 50 rpm, whereas Figs. 10 (d-f) depict results from equivalent experiments. The free-surfaces move smoothly and approach a steady-state after some twenty rotations of the vessel. Both wetting-and-peeling phenomena are observed at contact between the advancing and retreating surfaces and the vessel. Peeling is also observed at the contact point, between the dragging surface and the stirrer. However, for a constant limiting stretch factor α , peeling is not apparent in the simulations at the forward-driving surface near the stirrer, because of the lack of activity in this region due to the asymmetry of the geometry. Nevertheless, according to the experimental pictures, Figs. 10 (d-f), peeling does occur in this region near the stirrer. Such a localised phenomenon near the stirrer is difficult to capture accurately through simulation. However, this may be achieved by adopting a dynamic setting of the limiting stretch factor α for the contact position between forward surface and stirrer, and the dragging surface and stirrer. This dynamic setting, with α_{stir} -value varying from 1.3 for the outer stirrer section (narrow-gap) to 0.8 for the inner stirrer section (wide-gap), is chosen according to local dictates. The difference between computed results with static and dynamic setting of stretch factor α_{stir} is demonstrated in Fig.11. In the experimental pictures, Figs. 10 (d-f), it is apparent that there is little change in the surface profile along the length of the geometry, except for some meniscus effects (3D effects) at the flat ends of the geometry. The fluid is observed to climb up the ascending portion of the geometry and to be carried downward on the descending side, due to the forces generated by shear flow between the fluid and the wall. The simulation (2D) results match closely with the surface profile at the central plane of the experimental geometry. Note that in reality (experiment), a thin layer of

fluid is carried around by the geometry, diverging from the climbing portion of fluid and recombining with the fluid on the descending side. This feature is not accounted for in the simulation due to the manner of imposition of wetting-and-peeling (via a virtual gap at the fluid-boundary interface). There is a small drop from the initial level of the bulk of the fluid. This can be partly attributed to the absence of the volume of liquid taken up by the thin layer and partly due to fluid-vessel contact and adjustments (wetting and peeling).

5 Conclusions

The principal aim of this study, was to develop numerical algorithms to predict free-surface rotating flows in part-filled dough mixers. This included both horizontal and vertical vessel orientations, validating findings against experiments. This has been successfully accomplished. For the free-surface modelling, an arbitrary Lagrangian-Eulerian scheme has been employed, where both horizontal (2D) and vertical (3D) orientations have been considered. Novel strategies based on stretch-rate/stress, have been incorporated to model wetting-and-peeling of the surface at fluid-boundary contact. Experimental pictures of the surface profiles, obtained using laser scatter technology and high-speed photography, have compared well with the simulation results. A peeling apparatus has been designed to investigate peeling of dough from the surface of the mixing bowl. This has provided a measure of peeling stress, and calibration for the numerical computations. Torque-time trace, recorded from the experiments, has assisted in differentiating the different modes within the kneading process. The torque-time trace illustrates a periodic trend, which corroborates that observed within the numerical modelling.

In vertical-vessel orientation for a concentric stirrer location, parabolic surface deformation patterns were obtained. Steady surface orientations and transient evolution profiles have been closely validated between experiment and simulation. Results confirm wetting of fluid, rising at the vessel, and peeling of fluid (drop) at the stirrer. Local stress and stretch are computed from stretch-rate and found to be of the same order as the critical stress obtained from the experiments. Horizontal orientation of the mixer presents the more complex wetting and peeling circumstances. In the modelling, even the fine details of wetting and peeling on different sections of boundary may be captured by adopting location-dependent limiting stretch conditions. The techniques and procedures developed in this study are quite general and now sufficiently mature to enjoy more wide application.

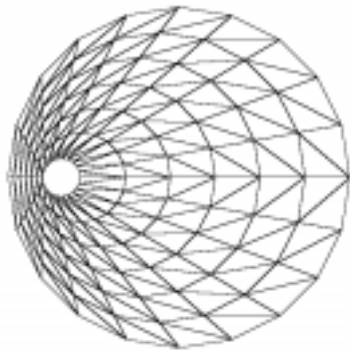
Acknowledgements

Financial support for this work, from BBSRC (grant no: 58/D08174), RHM Research, United Biscuits, Pilsbury Co., Mono Equipment and Sasib Bakeries, is acknowledged. The support work of Dr. D. Ding, especially in two-dimensional free surface, is also gratefully acknowledged.

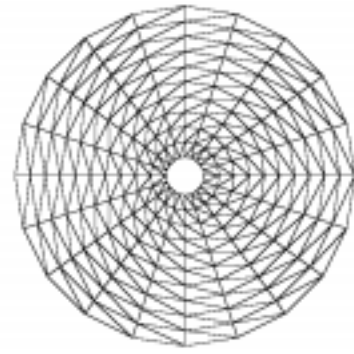
References

- [1] Harlow F.H. and Welch J.E., 1965, "Numerical calculation of time-dependent viscous incompressible flow of fluid with free-surface". *Phys. Fluids*, 8, pp. 2182-2189.
- [2] Hirt C.W. and Nichols B.D., 1981, "Volume of fluid method for the dynamics of free boundaries". *J. Comput. Phys.*, 39, pp. 201-225.
- [3] Gethin D.T., Lewis R.W. and Tadayan M.R., 1992, "A finite element approach for modeling metal flow and pressurized solidification in the squeeze casting process". *Int. J. Numer. Meth. Eng.*, 35, pp. 939-950.
- [4] Thompson E., 1986, "Use of pseudo-concentration to follow creeping viscous flows during transient analysis". *Int. J. Numer. Meth. Fluids*, 6, pp. 749-761.
- [5] Nassehi V. and Ghoreishy M.H.R., 1997, "Simulation of free surface flow in partially filled internal mixers". *Int. Poly. Process.*, 4, pp. 346-353.
- [6] Hirt C.W., Amsden A.A. and Cook J.L., 1974, "An Arbitrary Lagrangian-Eulerian computing method of all speeds". *J. Comput. Phys.*, 14, pp. 227-253.
- [7] Ramaswamy B., 1990, "Numerical simulation of unsteady viscous free surface flow". *J. Comput. Phys.*, 90, pp. 396-430.
- [8] Cochrane, T., Walters, K. and Webster, M.F., 1981, "On Newtonian and non-Newtonian flow in complex geometries". *Philos. Trans. Roy. Soc.*, A301, pp. 163-181.
- [9] Boger, D.V., 1982, "Circular entry flows of inelastic and viscoelastic fluids". *Advances in Transport Processes*, Wiley Eastern Ltd., pp. 43-104.
- [10] Evans, R.E. and Walters, K.W., 1985, "Flow characteristics associated with abrupt changes in geometry in the case of highly elastic liquids". *J. Non-Newtonian Fluid Mech.*, pp. 20, 11-29.
- [11] Prakash, S. and Kokini, J.L., 2000, "Estimation and prediction of shear-rate distribution as a model mixer". *J. Food Eng.*, pp. 135-148.
- [12] Dobraszczyk, B.J., 1997, "The rheological basis of dough stickiness". *J. Texture Studies*, 28, pp.139-162.
- [13] Ding D. and Webster M. F., 2000, "Three-dimensional numerical simulation of dough kneading" in Binding D., Hudson N., Mewis J., Piau J.M., Petrie C., Townsend P., Wagner M., Walters K. (Eds.), X111 *Int. Cong. On Rheol.*, Vol. 2, British Society of Rheology, Cambridge, UK, pp 318-320.
- [14] Couch M.A. and Binding D.M., 2000, "Experimental simulation of dough-kneading" in Binding D., Hudson N., Mewis J., Piau J.M., Petrie C., Townsend P., Wagner M., Walters K. (Eds.), X111 *Int. Cong. On Rheol.*, Vol. 2, British Society of Rheology, Cambridge, UK, pp 351-353.

- [15] Sujatha K.S., Ding D. and Webster M.F., 2001, "Modelling three-dimensional mixing flows in cylindrical-shaped vessels". ECCOMAS-2001, Swansea, UK.
- [16] Sujatha K.S. and Webster M.F., 2001, "Modelling three-dimensional rotating flows in cylindrical-shaped vessels". *Int. J. Num. Meth. Fluids* (submitted).
- [17] Couch M.A., Binding D.M., Sujatha K.S. and Webster M.F., 2001, "Experimental and numerical simulation of dough kneading in filled geometries". *J. Food Eng.* (submitted).
- [18] Hawken D. M., Tamaddon-Jahromi H. R., Townsend P., and Webster M.F., 1990, "A Tayllor-Galerkin-based algorithm for viscous incompressible flow". *Int. J. Num. Meth. Fluids*, 10, pp. 327-351.
- [19] Ding D., Townsend P., and Webster M. F., 1995, "On computations of two and three-dimensional unsteady thermal non-Newtonian flows". *Int. J. Num. Meth. Heat Fluid Flow*, 5, pp. 495-510.
- [20] Matallah H., Townsend P., and Webster M. F., 1998, "Recovery and stress-splitting schemes for viscoelastic flows". *J. Non-Newtonian Fluid Mech.*, 75, pp. 139-166.
- [21] Couch, M.A., Binding, D.M. (2000). *Experimental Simulation of Dough Kneading. Rheology 2000 - XIII Int. Congress on Rheology BSR Glasgow*, 2, 351-353.
- [22] Couch M.A. and Binding D.M., 2001, "An experimental study of the peeling of dough from solid surfaces". *J. Food Eng.* (submitted).
- [23] Baloch A. and Webster M.F., 2001, "Distributed parallel computation for complex rotational flows of non-Newtonian fluids, *Eng. Computations.* (submitted).
- [24] Baloch A., Grant P.W. and Webster M.F., 2001, "Parallel computation of two-dimensional rotational flows of viscoelastic fluids in a cylindrical vessel, *Int. J. Num. Meth. Fluids* (submitted).
- [25] Sujatha K.S. and Webster M.F., 2002, "Modelling free-surface flows in part-filled rotating vessels: vertical and horizontal orientations, *J. Fluids Eng.* (submitted).



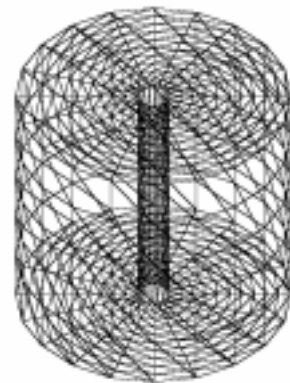
(a)



(b)



(c)



(d)

Figure 1. Meshes, (a-b), horizontal (2D); (c-d) vertical (3D) views.

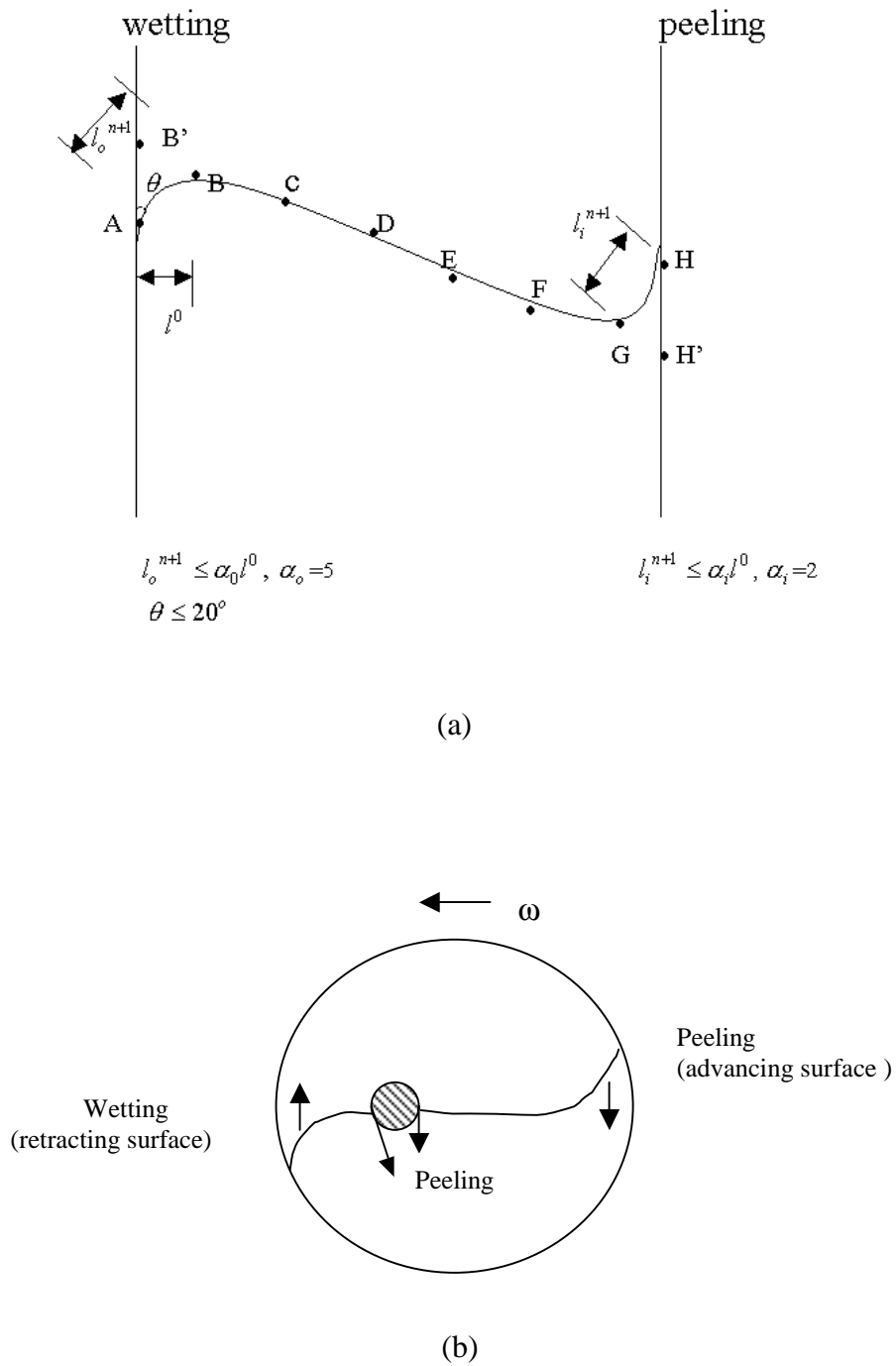


Figure 2. Schematic representation of wetting and peeling:
 (a) vertical orientation; (b) horizontal (r, θ) orientation.

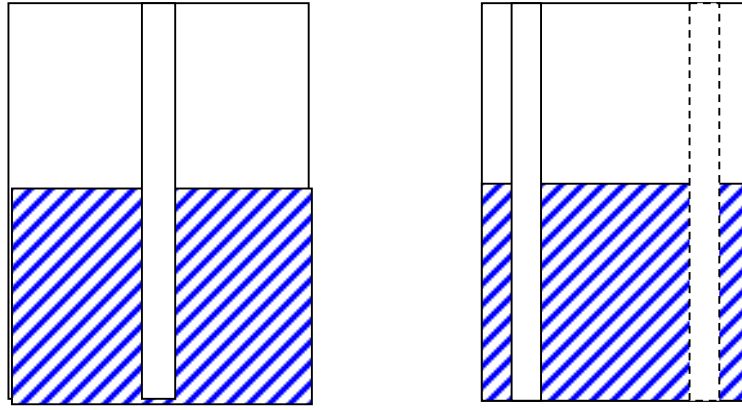


Figure 3. The concentric and eccentric geometries.

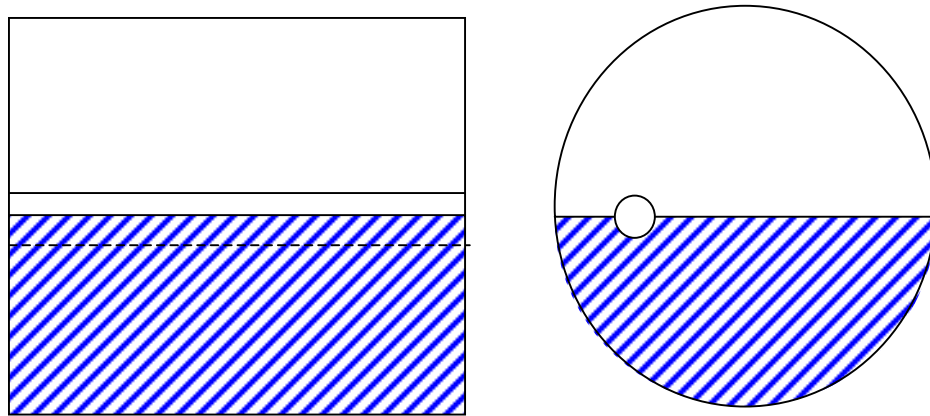
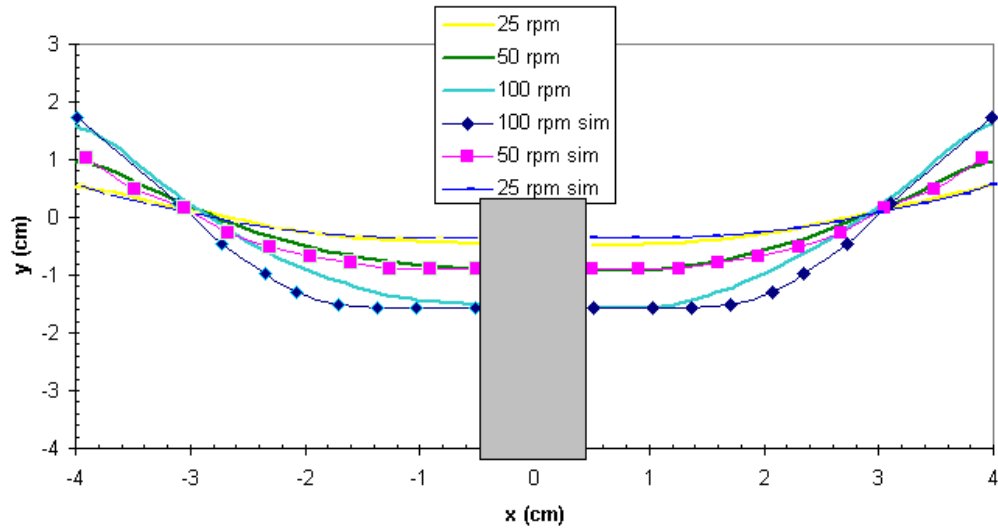
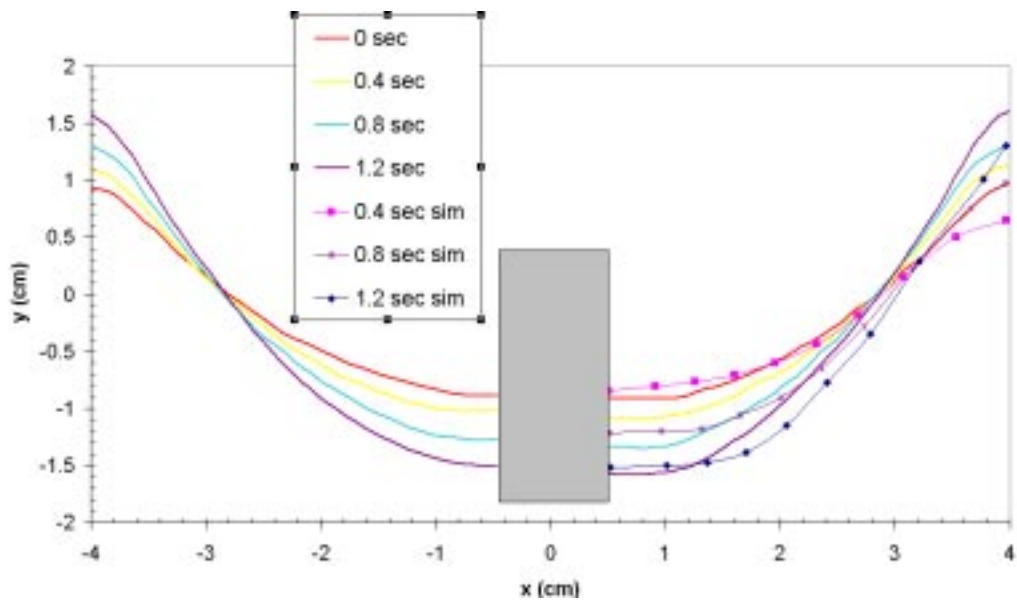


Figure 4. The eccentric geometry in horizontal orientation.

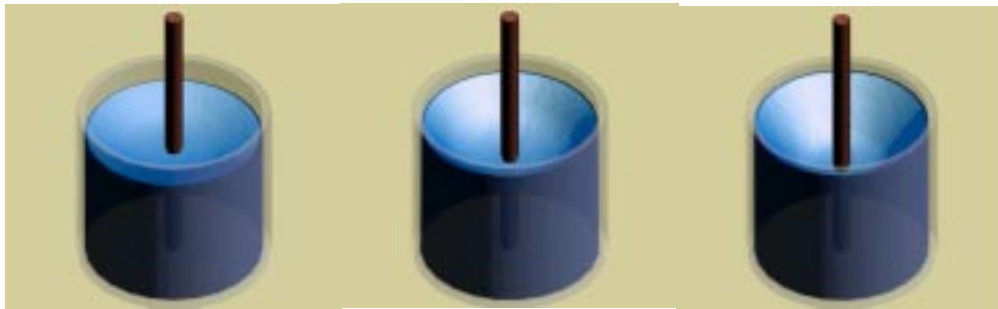


(a)

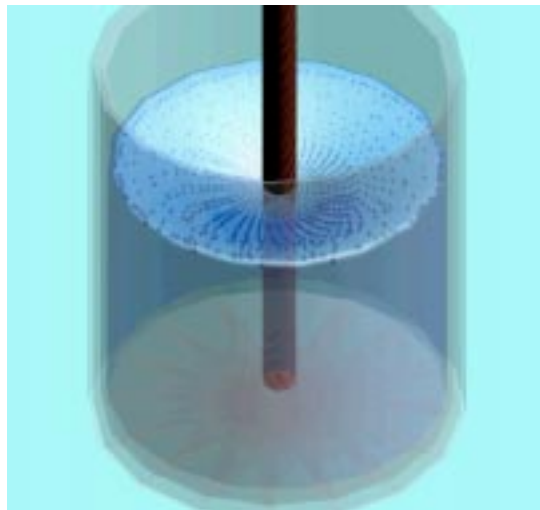


(b)

Figure 5. Surface positions, Simulation versus experiment, steady (a), ($Re=4, 8$ and 16), and transient rise (b), $Re=16$.



(a) $Re = 4$ (25 rpm) (b) $Re = 8$ (50 rpm) (c) $Re = 16$ (100 rpm)



(d) $Re=8$ (50 rpm)



(e) $Re = 4$ (25 rpm) (f) $Re = 8$ (50 rpm) (g) $Re = 16$ (100 rpm)

Figure 6. Surface patterns: increasing speeds, 3D mode, a-d) simulation, e-g) experiment; d) surface with particle positions.

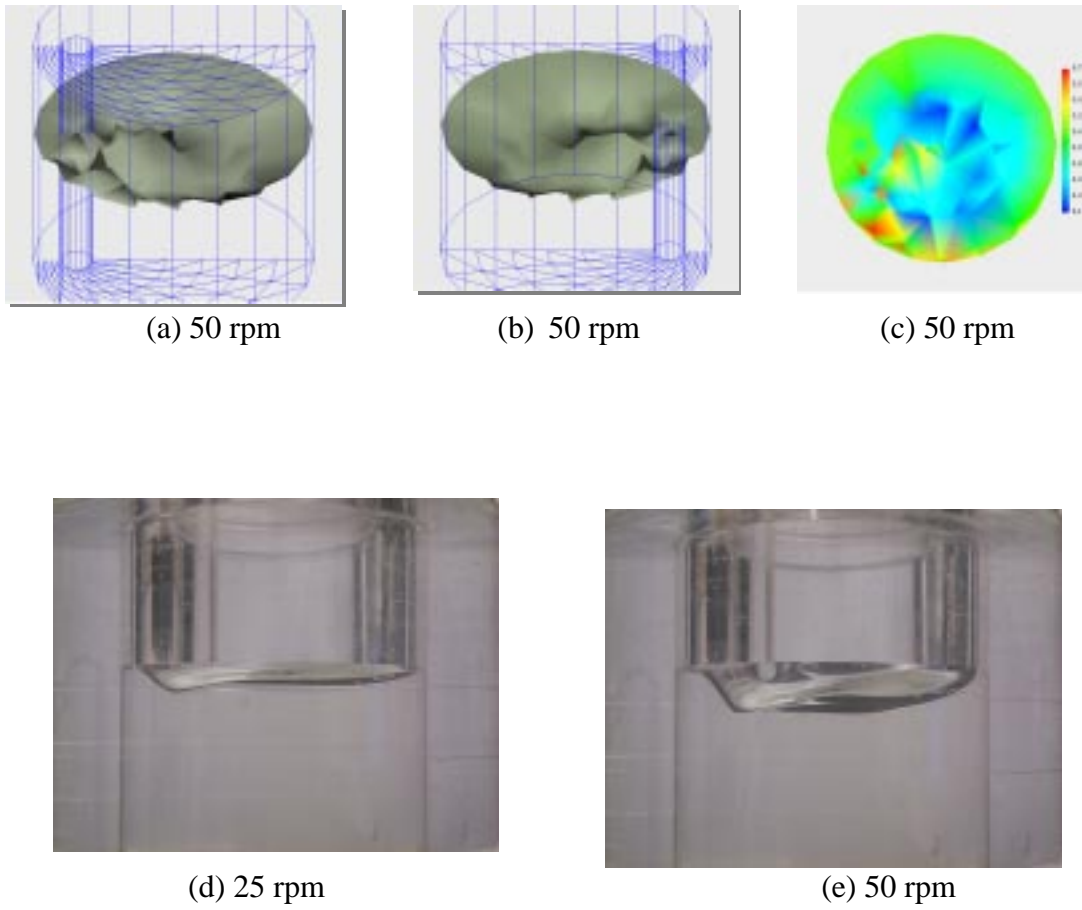


Figure 7. Steady free-surface profiles for eccentric, one-stirrer geometry: a-c) simulation; d,e) experiment.

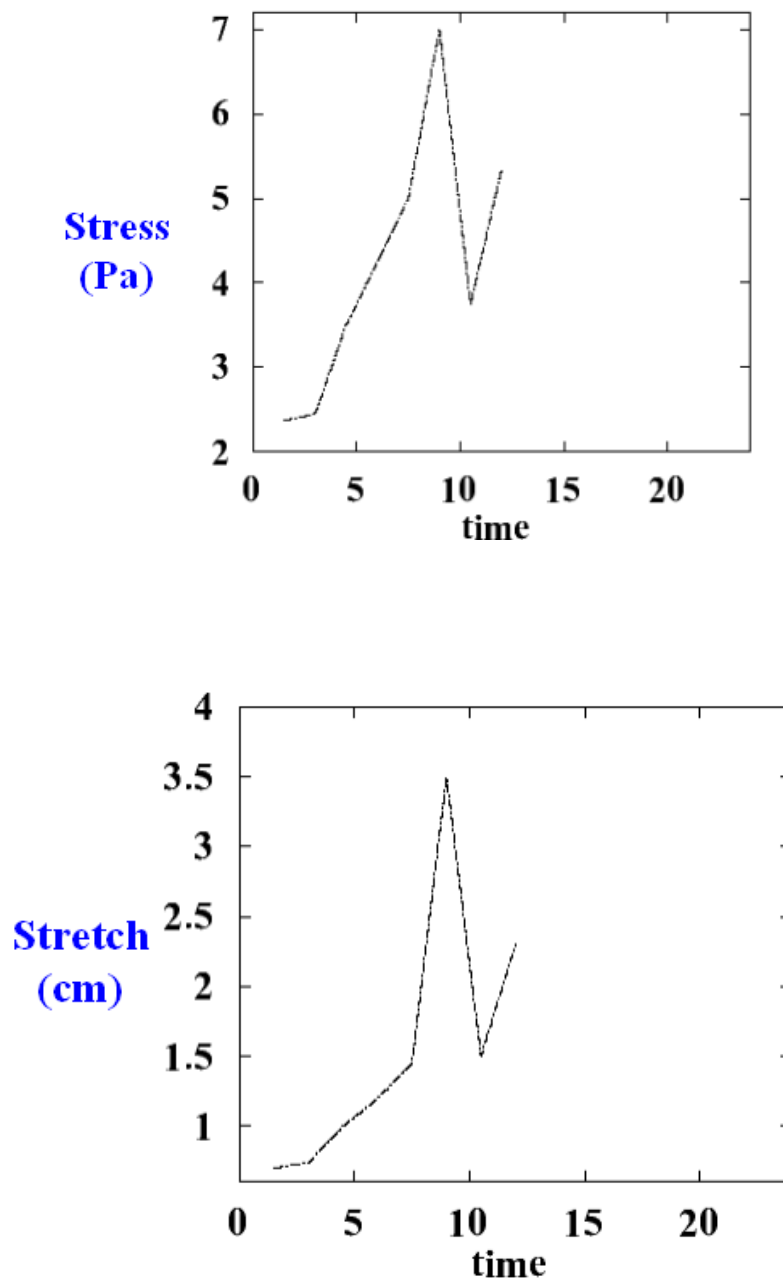
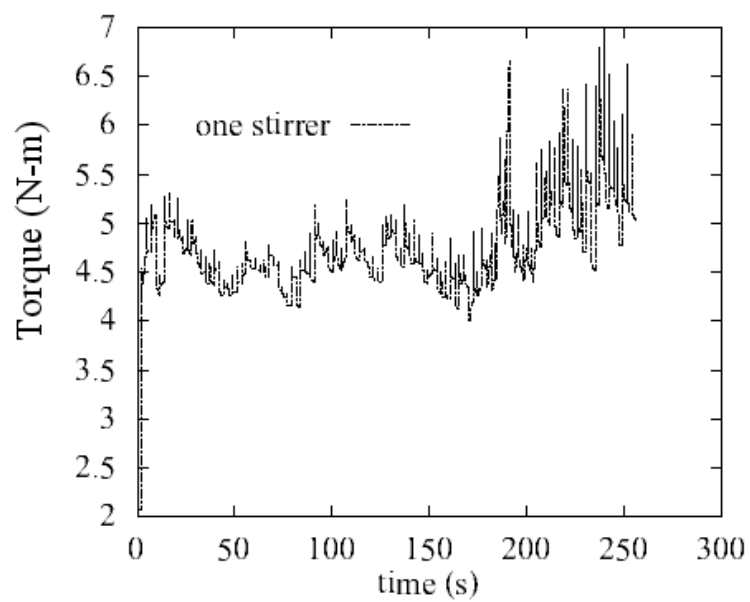
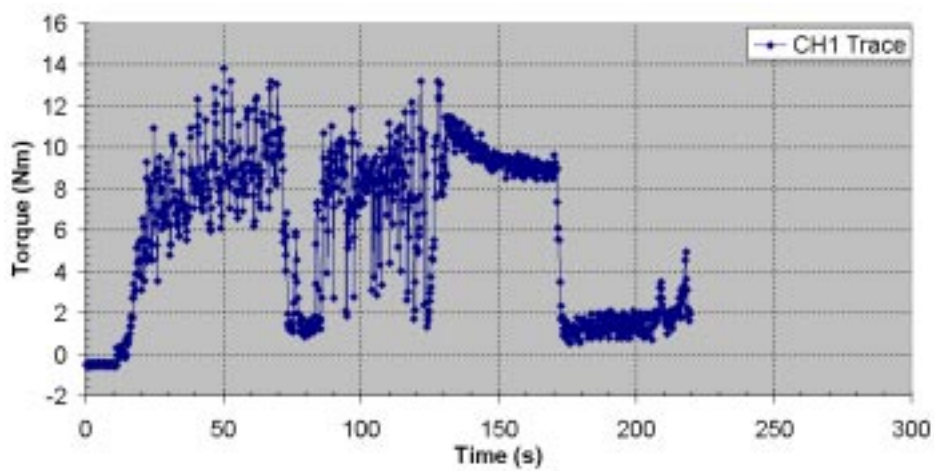


Figure 8. Variation of stress and stretch with time; 3D, Re= 8 (50 rpm).



(a)



(b)

Figure 9. Torque-time trace: a) simulation, b) experiment; single-rod, eccentric vertical-vessel, 3D, $Re=8$ (50 rpm).

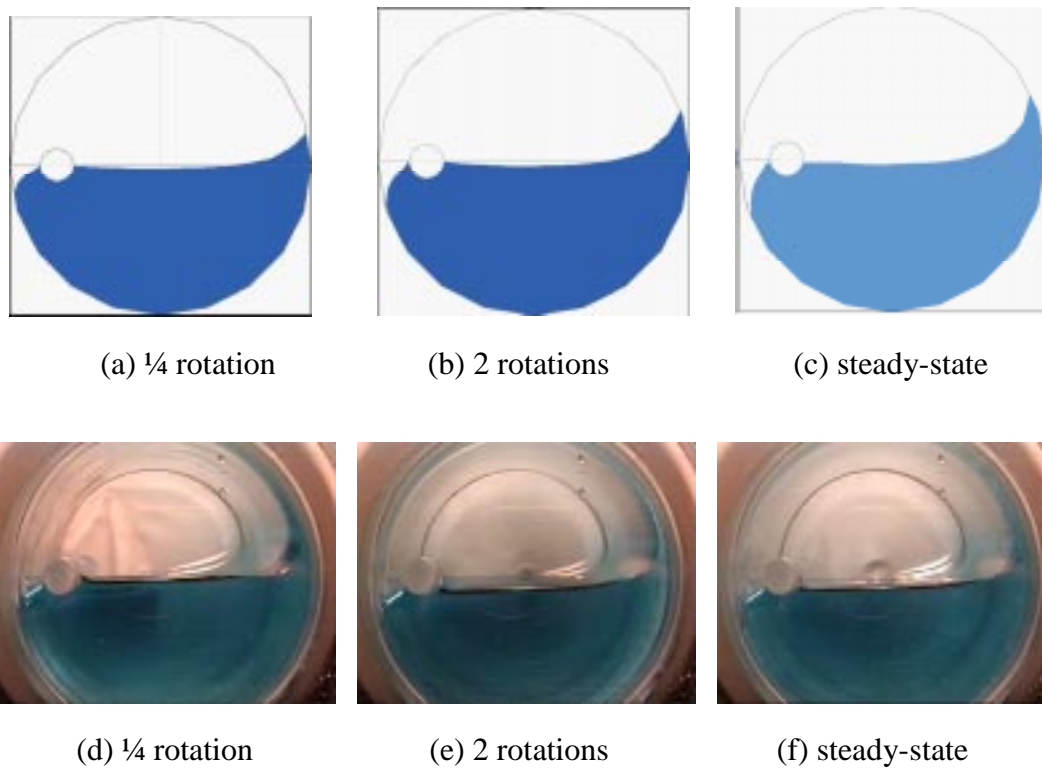


Fig. 10. Surface deformation patterns, temporal development, $Re = 8$ (50 rpm):
(a-c) simulation, (d-f) experiments.

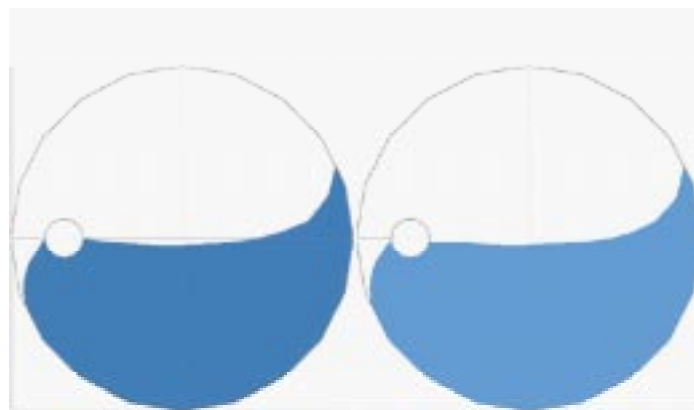


Figure 11. Steady-state surface positions, simulations, $Re = 8$ (50 rpm):
left $\alpha_{\text{stir}}=2$; right $\alpha_{\text{stir-outer}}=1.3$, $\alpha_{\text{stir-inner}}=0.8$